Spatiotemporal Model-Based Estimation of High-Density Atrial Fibrillation Activation Maps

Running title: Spatiotemporal Estimation of Atrial Fibrillation Activation Maps

Alejandro Alcaine[1,2], Natasja M. S. de Groot[3], Pablo Laguna[1,2], Juan Pablo Martínez[1,2], Richard P. M. Houben[4]

[1]BSICoS Group, Aragón Institute of Engineering Research (I3A), IIS Aragón, Universidad de Zaragoza, 50018, Zaragoza, Spain; [2]CIBER en Bioingeniería, Biomateriales y Nanomedicina (CIBER-BBN), 28029, Madrid, Spain; [3]Translational Electrophysiology Unit, Department of Cardiology, Erasmus Medical Center, PO Box 2040, 3000 CA, Rotterdam, The Netherlands; [4]2BMedical B.V., 6226 NA, Maastricht, The Netherlands.

Correspondence:

Richard P. M. Houben

2BMedical B.V.

Bergerstraat 2, 6226 NA, Maastricht, The Netherlands.

Phone: 0031 6 397 666 70

E-Mail: richard.houben@2bmedical.com

Document total words: 8578 (From Abstract to Reference section: 6534)

Abstract:

Examination of activation maps using multi-electrode array (MEA) sensors can help to understand the mechanisms underlying atrial fibrillation (AF). Classically, creation of activation maps starts with detection of local activation times (LAT) based on recorded unipolar electrograms. LAT detection has a limited robustness and accuracy, and generally requires manual edition. In general, LAT detection ignores spatiotemporal information of activation embedded in the relation between electrode signals on the MEA mapping sensor. In this work, a unified approach to construct activation maps by simultaneous analysis of activation patterns from overlapping clusters of MEA electrodes is proposed. An activation model fits on the measured data by iterative optimization of the model parameters based on a cost function. The accuracy of the estimated activation maps was evaluated by comparison with audited maps created by expert electrophysiologists during sinus rhythm (SR) and AF. During SR recordings, 25 activation maps (3100 LATs) were automatically determined resulting in an average LAT estimation error of -0.66 ± 2.00 ms and a correlation of $\rho_s = 0.98$ compared to the expert reference. During AF recordings (235 maps, 28226 LATs), the estimation error was -0.83 ± 6.02 ms with only a slightly lower correlation ($\rho_s = 0.93$). In conclusion, complex spatial activation patterns can be decomposed into local activation patterns derived from fitting an activation model, allowing the creation of smooth and comprehensive high-density activation maps.

Keywords: Activation Mapping, Atrial Fibrillation, Multi-Electrode Array Sensors, Normal Sinus Rhythm, Solid Angle, Uniform Double Layer, Unipolar Electrograms.

1. Introduction:

Atrial fibrillation (AF) is one of the most common arrhythmias, responsible for one third of all hospitalizations at cardiac arrhythmia units [1], with an increasing prevalence due to aging of the population[2,3]. Moe *et al.* [4] first proposed the wavelet hypothesis underlying the initiation and perpetuation of AF, describing the presence of multiple propagating wavelets sustaining the fibrillation process, validated later by Allessie *et al.* [5,6]. Other proposed mechanisms include driving foci, mainly located at the pulmonary veins [7], re-entrant circuits, rotors [8,9] and trans-mural conduction of fibrillation waves between epicardial and endocardial atrial layers [10,11]. However, mechanisms underlying the initiation and perpetuation of AF are not yet fully understood [8], limiting the optimal treatment of patients.

Activation mapping is the most commonly used method for visualization and study of cardiac arrhythmias [12]. During hemodynamically stable and regular tachycardia, activation maps can be created after sequential recording of electrograms (EGM) and detected local activation times (LAT) can be referred against a fiducial point in a simultaneously recorded surface or intracardiac signal [13]. However, during irregular tachycardia like AF, simultaneous mapping is needed due to the non-repetitive nature and complexity of the arrhythmia [8]. Multi-electrode mapping catheters such as PentaRay and Lasso (*Biosense Webster, Inc. Diamond Bar, CA, USA*) or the Constellation full contact basket catheter (*Boston Scientific, Inc. Natick, MA, USA*) lack spatial resolution during more complex activation of the atrium due to electrode sparsity and bad wall contact [14]. For high-density mapping of more complex AF, a high-density multi-electrode array (MEA) mapping sensor will be needed [8].

In this study, unipolar electrograms (u-EGM) were recorded using a MEA mapping sensor in direct contact to the epicardial wall of the atrium during open chest surgery. The

65 recorded signals are displayed in a matrix related to the location of the electrodes on the
66 MEA sensor. This will allow constructing activation maps which show the propagation of
67 cardiac activation [6,8].

68 The construction of activation maps involves several processing steps including
69 denoising, baseline correction, far field R-wave cancelation and detection of activation times
70 followed by an error rejection process. Detection of LATs is related to the u-EGM steepest
71 negative slope (dV/dt) as a result of an activation wave under-passing the recording
72 electrode [15,16]. Activation maps are constructed by combining LATs detected from each of
73 the electrodes on the mapping array. However, this procedure ignores the information
74 embedded in the morphology of the u-EGM signal, hence not used for the creation of high-
75 density activation maps.

76 Detailed cardiac electrophysiological modelling provides insight in the physiology
77 underlying cardiac arrhythmias and serves as a tool for a better diagnosis and interpretation of
78 experimental data [17]. Those models describe the ion currents flowing through the
79 myocardial cell membrane (e.g.[18,19]) embedded in realistic structures and geometries of
80 the human heart [17]. Less detailed models of cardiac propagation provide a less time-
81 consuming alternative to represent the cardiac activation propagation. Equivalent source
82 model uses current sources and densities to calculate the potentials, hence describing the
83 activation propagation as a uniform double layer (UDL) model [20].

84 In this paper, a unified spatiotemporal approach for estimation and construction of
85 high-density activation maps is presented. The proposed method fits an activation pattern
86 model to acquired cardiac activity in order to reconstruct the complete activation map as the
87 combination of contributions from different isotropic focal activation sources. The
88 contribution of each of the sources was determined by an iterative optimization process

modifying the UDL propagation model after comparing the modelled signals against u-EGM signals acquired during epicardial atrial mapping in sinus rhythm (SR) and AF. Finally, the complete activation map was reconstructed by combining individual solutions. Preliminary analysis of this approach has been reported in [21].

2. Materials and methods:

2.1. High-density atrial epicardium recordings:

The clinical data used in this study was obtained from a 61 years-old male patient with coronary artery disease, without a history of AF which echocardiographic examination revealed a normal left ventricular ejection fraction and normal atrial dimensions. The patient was admitted for open chest surgery at Erasmus Medical Center Rotterdam (Rotterdam, The Netherlands) in whom an intraoperative electrophysiological study was performed. The patient was informed and signed the consent form. During the intervention, a custom made high-density MEA mapping sensor (*Applied Biomedical Systems B.V., Maastricht, The Netherlands*) was positioned on the epicardial wall of the left and right atrium following a sequence of epicardial locations, as illustrated in Fig. 1(a). Datasets of high-density u-EGMs signals were acquired during SR and AF.

Figure 1 here

Fig. 1: Schematic of the mapping procedure in posterior view: (a) Anatomical location of the MEA sensor in the atrium and (b) MEA sensor used for mapping procedure. CS: Coronary Sinus, CT: Crista Terminalis, IVC: Inferior Vena Cava, LA: Left Appendage, LBB: Left Bachmann Bundle, LPV: Left Pulmonary Vein, RA: Right Appendage, RBB: Right Bachmann Bundle, RPV: Right Pulmonary Vein, SVC: Superior Vena Cava.

The custom MEA sensor measures 3.0×1.4 cm, is composed by 128 circular gold plated electrodes (2 mm inter-electrode distance, 1 mm diameter) organized in an 8×16 rectangular grid. Electrode channels corresponding to each corner of the mapping array were not available for mapping and were reserved for storing surface ECG, reference and calibration signals, resulting in 124 u-EGM signals available for analysis (Fig. 1(b)). The acquired u-EGM signals were band-pass filtered (1-500 Hz) sampled and digitized at 1 kHz. The recording length during SR episodes was 5 s and 10 s during AF episodes.

Automatic LAT detection was performed off-line after the procedure using a wavelet-based algorithm [22] and subsequently audited by an expert electrophysiologist blind to the detection outcome of this work. Therefore, the resulting LATs were considered as *"ground truth"* for performance evaluation of the proposed algorithm.

2.2. Algorithm overview and notation:

Before algorithm starts, a 100 ms signal excerpt that includes a complete activation across the MEA sensor is selected and the mapping array is segmented in 44 overlapped groups of 5×5 electrodes (area 64 mm^2), being this the size of the analysing mask in this work. A comprehensive flow of the processing steps is described below:

```
L1: For each 5×5 group of electrodes:
```

1. Estimate conduction velocity and initial focus location, which is considered the source for this estimation.
2. Generate activation pattern and modelled u-EGMs.
3. Compare measured against modelled u-EGMs.

L2: While the similarity is below a given threshold or the maximum number of iterations is not reached:

a) Compute new focus location for next iteration.

b) Generate new activation pattern and modelled u-EGMs.

c) Compare measured against modelled u-EGM signals.

End of loop L2.

End of loop L1. Go to step 1 unless all 5x5 groups have been already analysed.

4. Activation map reconstruction.

For notation, $s_i[n]$ stands for the recorded u-EGM signal corresponding to the i th electrode, $i = 1...25$, from the 5×5 group under analysis and $\hat{s}_i[n]$ denotes the modelled u-EGM signal corresponding to the same electrode located in the cardiac tissue model.

2.3. Activation pattern and tissue model:

The basic activation pattern can be generalized as a single focal point generating an activation wavefront concentrically spreading with a uniform conduction velocity. In a 2-dimensional plane, the wavefront coordinates $\mathbf{w}_{\mathbf{f},v}[n,\theta] = [w_x[n,\theta], w_y[n,\theta]]^{\mathrm{T}}$ created by a circular activation pattern with center focus location $\mathbf{f} = \left[f_x, f_y\right]^{\mathrm{T}}$ at a time instant n; can be described by the parametric form:

$$\mathbf{w}_{\mathbf{f},v}[n,\theta] = \begin{bmatrix} w_x[n,\theta] \\ w_y[n,\theta] \end{bmatrix} = \begin{bmatrix} f_x \\ f_y \end{bmatrix} + v \cdot n \cdot \begin{bmatrix} \cos(\theta) \\ \sin(\theta) \end{bmatrix}, \quad (1)$$

where $\theta = \left[0, 2\pi\right)$ and v stands for the conduction velocity of the medium. Note that

$\mathbf{w}_{\mathbf{f},v}[n,\theta]$ is the expression of a circumference of radius $v \cdot n$ centred at $\mathbf{f}$. Hence, (1) defines a circular activation pattern from a single focus, becoming a planar wave when the focus is located far away from the observer scope.

The activation pattern was introduced into a UDL model using the boundary element method [20]. The UDL models a square planar slice of atrial tissue of 12×12 mm and 2 mm thick conform to the average thickness of the human atria [23]. Since no EGMs from the endocardial wall were recorded, epicardial and endocardial conduction velocity was assumed to be equal [24]. Consequently, the modelled activation propagates in parallel and at the same velocity in both endocardial and epicardial side of the UDL model.

2.4. EGM signal modelling:

A virtual MEA sensor (v-MEA) with 5×5, 2 mm spaced, circular electrodes was placed on the epicardial side of the UDL enabling calculation of electrical activity during activation. Each i th virtual electrode of the v-MEA has a spatial location $\mathbf{e}_i = [x_i, y_i]^{\mathrm{T}}$. The infinite medium potential generated by a UDL at time instant n and position $\mathbf{e}_i$ is given by [20]:

$$\hat{s}_i[n] = -\frac{V_d}{4\pi}\Omega_{\mathbf{e}_i}[n], \qquad (2)$$

where V_d stand for a constant value called *double layer strength* of the UDL [20] and $\Omega_{\mathbf{e}_i}[n]$ stands for the solid angle of the surface created by the activation wavefront $\mathbf{w}_{\mathbf{f},v}[n,\theta]$ and subtended within the UDL at $\mathbf{e}_i$, as illustrated in Fig. 2. This solid angle $\Omega_{\mathbf{e}_i}[n]$ can be computed numerically by dividing the wavefront surface into triangular elements and summing the solid angles subtended by each surface element, using the plane triangle formula [25].

Figure 2 here

Fig. 2: Schematic in: (a) perspective view and (b) lateral view, of the solid angle $\Omega_{\mathbf{e}_i}[n]$ obtained at electrode position $\mathbf{e}_i$ from a circular activation pattern $\mathbf{w}_{\mathbf{f},v}[n,\theta]$ subtended within a UDL shown as a closed grey strip.

Equation (2) describes the electrophysiological behaviour of local u-EGMs recorded from the myocardium. The potential $\hat{s}_i[n]$ increases when the activation wavefront approaches the recording electrode, shows a fast downward slope when the wave underpasses the electrode and goes back to baseline when the wave passes away [13,15,20]. The amplitude of this fast downwards slope is proportional to the *double layer strength* V_d [20], hence it can be estimated from the measured u-EGM signals as the mean value of all amplitude difference between the positive and negative deflection (i.e., the R-wave and S-wave, respectively). This constant value does not affect the spatiotemporal features of $\hat{s}_i[n]$ (i.e., the LAT and wave morphology) hence having been set arbitrarily in this work to $V_d = 1$.

2.5. Estimation of tissue conduction velocity:

To use the propagation model (1), the conduction velocity of the cardiac tissue v needs to be estimated from recorded u-EGMs. Estimation of conduction velocity from invasive data is an already addressed problem (e.g. in [6,26–28]), although difficult due to the spatiotemporal changes of cardiac tissue properties, especially during irregular tachycardias [26].

Estimation of conduction velocity based on LATs can be sensitive to detection errors. Therefore, an alternative approach is used in this work inspired in that presented by Fitzgerald *et al.* [27]. The time delay δ_i between each u-EGM $s_i[n]$ and the central electrode of the 5×5 group being analysed $s_r[n]$ is obtained by maximizing the normalized cross-covariance function:

196 $$\delta_i = \underset{m}{\operatorname{argmax}}\{C_{i,r}[m]\}, \quad (3)$$

197 $$C_{i,r}[m] = \frac{\sum_n (s_i[n]-\bar{s}_i)(s_r[n-m]-\bar{s}_r)}{\sqrt{\sum_n (s_i[n]-\bar{s}_i)^2 \sum_n (s_r[n]-\bar{s}_r)^2}}, \quad (4)$$

198 where $\bar{s}_i$ and $\bar{s}_r$ stand for the mean value $s_i[n]$ and $s_r[n]$, respectively; and m represents the
199 time lag between signals.

200 The next step involves the estimation of the conduction velocity for the 5×5 electrode
201 analysing mask while avoiding the possible effect of electrode bad contact, noise or
202 conduction blocks. A biquadratic model is fitted to the delays measured from each 3×3 sub-
203 group of electrodes at $k = 1...4$ corners of the complete 5×5 group following [26]:

204 $$D^k(x,y) = a_1 + a_2 x + a_3 y + a_4 xy + a_5 x^2 + a_6 y^2, \quad (5)$$

205 where $a_1 \ldots a_6$ are the coefficients of the biquadratic model obtained in the least square sense
206 [26]. Only those fitted models with RMSE ≤ 1.5 ms were considered valid [24]. Then, the
207 velocity vector field can be obtained by partial differentiation of $D^k(x,y)$ following [26]:

208 $$\hat{\mathbf{v}}^k(x,y) = \begin{bmatrix} \frac{dx}{dD^k} \\ \frac{dy}{dD^k} \end{bmatrix} = \begin{bmatrix} \frac{\dot{D}_x^k}{\left(\dot{D}_x^k\right)^2 + \left(\dot{D}_y^k\right)^2} \\ \frac{\dot{D}_y^k}{\left(\dot{D}_x^k\right)^2 + \left(\dot{D}_y^k\right)^2} \end{bmatrix}, \quad (6)$$

209 where $\dot{D}_x^k = \partial D^k(x,y)/\partial x$ and $\dot{D}_y^k = \partial D^k(x,y)/\partial y$. The estimated velocity vectors $\hat{\mathbf{v}}_i^k$ were
210 obtained by evaluating (6) at each electrode location $[x_i, y_i]^{\mathrm{T}}$. Then, for each k th 3×3 sub-
211 group of electrodes, an estimated conduction velocity is obtained for all $i \in k$ th corner as:

212 $$\hat{v}_k = median\left\{\left\|\hat{\mathbf{v}}_i^k\right\|\right\}. \quad (7)$$

213 Finally, the conduction velocity $\hat{v}$ for the complete 5×5 group of electrodes is

214 estimated by averaging $\hat{v}_k$ from each of the $K \leq 4$ corners with valid model fitting:

215 $$\hat{v} = \frac{1}{K}\sum_{k=1}^{K} \hat{v}_k \,. \qquad (8)$$

216 **2.6. Initial focus location:**

217 The focus location $\mathbf{f}$ in (1) will be estimated by the iterative algorithm introduced in section

218 2.2. The initialization process of $\mathbf{f}$ (step 1) is explained in this section.

219 *Figure 3 here*

220 **Fig. 3:** R-S relation evolution with distance to the activation focus: The u-EGM activation

221 measured at point (a) has nearly QS morphology (R^{i}_{RS}=-0.9) that turns into a RS morphology

222 as points (b) and (c) are distal from the source of activation (star). The grey dashed line

223 indicates the zero level. Curved lines show the evolution of the activation wavefront with

224 time in 5 ms steps.

225 The relation between the amplitude of the positive deflection (R-wave) and negative

226 deflection (S-wave) of the u-EGMs is influenced by wavefront curvature and distance to the

227 source of activation [13,24]. A QS morphology (i.e., absence of R-wave) indicates that the

228 electrode is located at the origin of the activation whereas RS morphology (i.e., equal R-wave

229 and S-wave amplitudes) indicates activation by a planar wave as illustrated in Fig. 3 [13]. In

230 order to take into account this phenomenon, for each i th electrode signal $s_i[n]$, the R-S

231 relation has been quantified as the difference between R-wave and S-wave amplitude

232 normalized by the peak-to-peak amplitude of the u-EGM signal [24]:

$$\mathrm{R}_{RS}^{i} = \frac{|R_i| - |S_i|}{|R_i| + |S_i|}, \tag{9}$$

were R_i and S_i stand for the R-wave and S-wave amplitudes of $s_i[n]$. R_{RS}^{i} ranges from -1 to 1, where negative values show predominance of S-wave over R-wave and vice versa [24]. Therefore, the initial focus $\mathbf{f}_0$ is set to the location of the electrode $i_{\min}$, which is activated earliest and has the most negative R-S relation, being estimated with a combined criterion:

$$i_{\min} = \underset{i}{\operatorname{argmin}}\left\{\delta_i + \mathrm{R}_{RS}^{i}\right\}. \tag{10}$$

2.7. Model optimization algorithm:

An iterative algorithm modifies $\mathbf{f}$ optimizing the fitting of the u-EGM signals derived from the propagation model (1) to the recorded data, while the conduction velocity $\hat{v}$ estimated in section 2.5 is unmodified.

The focus location is initialized at $\mathbf{f}_0$ and updated in each iteration l following

$$\mathbf{f}_{l+1} = \mathbf{f}_l + \Delta \cdot \mathbf{u}_l \cdot \Delta_t, \tag{11}$$

where Δ represents the update step, Δ_t the signal time resolution and $\mathbf{u}_l$ is the unit update vector towards the direction that improves the synchronization between the modelled and recorded u-EGMs. The update step is set up as $\Delta = \hat{v}$ therefore, in each iteration, $\mathbf{f}$ changes according to the distance that the activation wavefront travels in Δ_t ms. A schematic of this model optimization is shown in Fig. 4.

Figure 4 here

Fig. 4: Schematic of the model optimization algorithm: signals are derived from the modelled propagation pattern in test and compared against the measured u-EGM signals. The algorithm

253 decides a new focus location and the new pattern is tested. Direction vectors $\mathbf{r}_d$, $d = 1...4$,

254 connect the center of each 2×2 corner group of electrodes G_d (indicated by dashed squares)

255 to the activation focus $\mathbf{f}_l$. Vector $\mathbf{u}_{l+1}$ stands for the update vector for the next iteration. The

256 signal amplitudes were scaled for visualization purposes as indicated in method section 2.4. Note:

257 Characters with arrows appear boldface in text.

258 Synchronization between recorded and modelled u-EGMs is measured by the delay τ_i

259 obtained by maximizing the normalized cross-covariance function:

260 $$\tau_i = \underset{m}{\operatorname{argmax}}\{C_i[m]\}, \quad (12),$$

261 $$C_i[m] = \frac{\sum_n (\mathrm{s}_i[n] - \bar{s}_i)(\hat{s}_i[n-m] - \hat{\bar{s}}_i)}{\sqrt{\sum_n (\mathrm{s}_i[n] - \bar{s}_i)^2 \sum_n (\hat{s}_i[n] - \hat{\bar{s}}_i)^2}}, \quad (13)$$

262 where $\bar{s}_i$ and $\hat{\bar{s}}_i$ stand for the mean value $s_i[n]$ and $\hat{s}_i[n]$, respectively; and m represents the

263 time lag between signals.

264 Then, each 2×2 sub-group of electrodes G_d, $d = 1...4$, located at the corners of the

265 complete 5×5 group of electrodes under analysis (indicated within dashed squares in Fig. 4)

266 has a *"median sub-group delay"* defined as:

267 $$\tilde{\tau}_d = \underset{i \in G_d}{median}\{\tau_i\}. \quad (14)$$

268 On the other hand, the director vector from each sub-group G_d to the focus $\mathbf{f}_l$ is:

269 $$\mathbf{r}_d = \frac{\mathbf{f}_l - \mathbf{g}_d}{\left\|\mathbf{f}_l - \mathbf{g}_d\right\|}, \quad (15)$$

270 where $\mathbf{g}_d$ stands for the center coordinates of G_d.

Finally, the unit update vector $\mathbf{u}_l$ for the next iteration is determined by:

$$\mathrm{u}_l = \sum_{d=1}^{4}\left(\frac{\widetilde{\tau}_d}{\sum_d |\widetilde{\tau}_d|}\mathbf{r}_d \right), \tag{16}$$

$$\mathbf{u}_l = \frac{\mathrm{u}_l}{\|\mathrm{u}_l\|}, \tag{17}$$

whose direction depends of the sign of $\widetilde{\tau}_d$.

This process is repeated until a cost function Q exceeds a threshold or the maximum number of iterations is reached. The cost function Q is defined as:

$$Q = \underset{i}{mean}\{C_i[0]\}, \tag{18}$$

where $C_i[0]$ stands for the normalized cross-covariance value between the i th recorded and modelled u-EGM signals at zero delay, i.e., a measure of morphology similarity and synchronization. Therefore, Q can be interpreted as the average resemblance level between recorded and modelled signals given by the activation pattern in test.

When $Q \geq 0.85$, the algorithm is terminated. In case the algorithm meets the maximum number of iterations without reaching the threshold for Q, the solution is given by the location $\mathbf{f}_l$ with maximum Q. The algorithm embeds protection against solution oscillations to avoid local maxima solution by means of *inertia movements* (increasing Δ by 10% during a maximum of 5 iterations while Q value is not increasing using the last valid update vector $\mathbf{u}_{l-1}$) and *random transition vectors* (random movements of $\mathbf{f}_l$ in perpendicular directions to $\mathbf{u}_l$ when inertia vectors do not reduce Q after 5 iterations) which replace the update term $\Delta \cdot \mathbf{u}_l$ in (11).

290 Then, for each 5×5 group of electrodes, the outcomes of the algorithm are the
291 estimated conduction velocity $\hat{v}$, the final focus location $\mathbf{f}_l$ and the resulting value of Q
292 which evaluates the solution fitting. Additionally, "*loci maps"* are built by representing the
293 focus location $\mathbf{f}_l$ for each 5×5 group of electrodes in the MEA.

294 **2.8. Activation map reconstruction:**

295 After analysing all the 44 5×5 groups of electrodes in the complete 8×16 MEA sensor, the
296 activation sequence is obtained as follows.

297 Each j th electrode, $j = 1...124$, of the MEA sensor lies in $h = 1...h_j$ different 5×5
298 groups of electrodes, and therefore has $h_j \leq 20$ different LAT estimates $n_j(1)...n_j(h_j)$ and
299 cost function values $Q_j(1)...Q_j(h_j)$. Each n_j was identified by the maximum negative slope
300 of the modelled signal $\hat{s}_{j,h}[n]$ from the j th electrode contained in the h th 5×5 group. Where
301 each $\hat{s}_{j,h}[n]$ is obtained following (2) after the substitution of $\hat{v}_h$ and $\mathbf{f}_{l,h}$ in (1). The final
302 LAT estimate $\hat{n}_j$ for each j th electrode is obtained as the nearest integer of the weighted
303 averaging of the individual LAT estimates using Q_j as weights:

304 $$\hat{n}_j = \frac{\sum_{h=1}^{h_j} Q_j(h) \cdot n_j(h)}{\sum_{h=1}^{h_j} Q_j(h)}, \qquad (19)$$

305 For robust LAT estimation during AF recordings, the number of solutions taking part
306 of the map reconstruction in (19) were limited using a threshold ξ obtained as:
307 $\xi = \min\{\mu_Q - 2\sigma_Q, 0.55\}$, where μ_Q and σ_Q stand for the mean and standard deviation (SD)
308 of the Q values for all the 44 5×5 electrode groups. Therefore, if $Q_j(h) \leq \xi$, the activation

time is not considered in the computation of (19). The value 0.55 is set empirically as a minimum value of Q to consider a reliable LAT solution.

2.9. Evaluation protocol:

The evaluation of the proposed algorithm is performed by a comparison of the estimated LATs with those audited by an expert electrophysiologist showing this comparison error as mean ± SD.

Figure 5 here

Fig. 5: Representative examples of the atrial activity complexity classification proposed in this paper. Reference against estimated activation maps were shown in: (a) Normal sinus rhythm (NSR) activity (error: -0.31 ± 0.93 ms, area: 100 %), (b) abnormal sinus rhythm (ASR) activity (error: -0.23 ± 3.5 ms, area: 100 %), (c) single atrial fibrillation wavefront (SAFW) activity (error: -0.03 ± 2.96 ms, area: 100 %), (d) breakthrough (BT) activity (error: -0.27 ± 2.59 ms, area: 100 %), (e) atrial fibrillation wave fusion (AFWF) activity (error: -0.12 ± 1.73 ms, area: 100 %), (f) dissociated atrial activity due to a line of block (LB) (error: 0 ± 13.52 ms, area: 95.97 %) and (g) complex atrial fibrillation (CAF) activity (error: -5.3 ± 10.55 ms, area: 80.17 %). LATs are color-coded from red (earliest) to pink (latest) in 10 ms isochrones. In case of no LAT could be identified at one electrode location, a cross is used.

Activation maps were studied in function of the activation pattern complexity and classified into one of the following 7 degrees, illustrated in Fig. 5:

1. Normal sinus rhythm (NSR): Normal propagation of a single wavefront within the mapping catheter during SR.

2. Abnormal SR (ASR): Abnormal propagation of one or more wavefronts within the mapping catheter during SR.

3. Single atrial fibrillation wavefront (SAFW): Single AF wavefront propagating within the mapping catheter whose origin is located outside the mapping array.

4. Breakthrough (BT): Concentric AF propagation wavefront whose focus is located within the mapping array [11].

5. Atrial fibrillation wave fusion (AFWF): Two separated wavefronts collide and fuse into a single wavefront.

6. Line of Block (LB): A line of block is present in the propagation pattern of the mapping catheter creating longitudinal dissociation of wavefronts traveling at different velocities and/or directions [10].

7. Complex AF (CAF): Chaotic activation with wave interruption and multiple lines of block.

Since LATs have an ordered nature (i.e., from earliest activated to latest activated electrode), Spearman's rank correlation ρ_s has been computed for assessing the performance of the proposed method. Additionally, Lin's concordance correlation factor ρ_c [29] and Bland-Altman analysis were used to assess agreement between the measurements. A p-value ≤ 0.05 was required for considering statistical significance. Sensitivity Se and positive predictive value P^+ of the detection have been computed as:

$$Se = \frac{TP}{TP + FN}, \tag{20}$$

$$P^+ = \frac{TP}{TP + FP}, \tag{21}$$

where TP stands for the number of true detections, FN stands for the number of missed

352 detections and FP stands for the number of false detections. A tolerance of ± 5 ms respect to
353 the expert reference LATs was used to consider a true detection.

354 **3. Results:**

355 **3.1. Analysis of SR recordings:**

356 Table 1 summarizes the results obtained during SR. Note that in contrast to recordings at *RA1*
357 to *RA3*, recording at *RA4* shows abnormal SR activity suggesting a stable functional re-
358 entrant circuit (illustrated in Fig. 5(b)) which is present during the complete recording time.

359 *Table 1 here*

360 **Table 1:** Detection error (mean ± SD), sensitivity and positive predictive value of comparing
361 estimated LATs with the manual reference in SR recordings. N/A stands for Not Applicable.

362 The global error obtained with the proposed method is -0.66 ± 2.00 ms across 3100
363 LAT measurements, thus covering the 100 % of the sensor area. A high level of agreement is
364 confirmed by high Spearman's correlation ($\rho_s = 0.98, p < 0.01$) and high Lin's concordance
365 correlation factor ($\rho_c = 0.98, p < 0.01$) as shown in Fig. 6. Bland-Altman analysis shows
366 (Fig. 6(b)) no trend in LAT estimation (Pearson's $\rho = -0.01,\ p = 0.73$). Moreover, the
367 detection performance is also high with $Se = 100$ % and $P^+ = 97.84$ %. Those observations
368 confirm the high agreement between measurements during SR as illustrated by activation
369 maps shown in Fig. 5(a)-(b).

370 *Figure 6 here*

371 **Fig. 6:** Agreement evaluation between reference and estimated LATs during SR: (a)
372 Reference vs. estimated LATs plot for Lin's concordance correlation factor ρ_c where pink

line indicates the unit slope and (b) Bland-Altman plot where red solid line indicates mean error and red dashed lines show mean ± 2SD of the error.

3.2 Analysis of AF recordings:

Table 2 summarizes the results obtained using the proposed method during AF. Note that LB and CAF complexity levels were only present at recording *RA1*. The global error obtained by evaluating a total of 28226 different LATs is -0.83 ± 6.02 ms covering almost the complete MEA sensor area (97.99 ± 7.66 %) having high agreement with manual annotations indicated by Spearman's $\rho_s = 0.93$ and Lin's concordance correlation factor $\rho_c = 0.90$ ($p < 0.01$ both). On the other hand, the detection performance is also high with $Se = 97.80$ % and $P^+ = 88.36$ %. The Bland-Altman analysis (Fig. 7(f)) illustrates this agreement and shows a slight trend of the proposed method towards over-estimation of early LATs and sub-estimation of late LATs (Pearson's $\rho = 0.21,\ p < 0.01$). Representative examples of activation map reconstruction during AF are shown in Fig. 5(c)-(g).

Table 2 here

Table 2: Detection error (mean ± SD), sensitivity and positive predictive value of comparing estimated LATs with the manual reference per AF recording at different levels of AF complexity. N/A stands for Not Applicable.

Figure 7(a)-(e) shows individual LATs agreement analysis for each AF complexity level proposed in this paper. A high level of agreement is found for SAFW, BT and AFWF. However, LB and CAF show lower level of agreement (Fig. 7(d)-(e)).

Figure 7 here

Fig. 7: Agreement evaluation between reference and estimated LATs during AF at different complexity levels including (a) SAFW, (b) BT, (c) AFWF, (d) LB (e) CAF and (f) all LATs studied in this work. In each pair of panels, left shows reference vs. estimated LAT plot for Lin's concordance correlation factor ρ_c (pink line indicates the unit slope) and the right panel shows Bland-Altman plot (red solid line indicates mean error and red dashed lines show mean ± 2SD of the error).

3.3 The *"loci maps"*:

Aside from the activation map reconstruction, an interesting result of the proposed method is the estimation of the activation pattern origin $\mathbf{f}$ for a given 5×5 group of electrodes of the MEA sensor. Therefore, construction of *"loci maps"* is possible by plotting all estimated focus location $\mathbf{f}$ across the MEA sensor. Fig. 8 shows examples of these *loci maps* from different activation patterns merged with the activation map. Note that *loci maps* spatially follow the potential activation wavefront evolution, providing extra information to complement the activation map.

Moreover, these *loci maps* can show different wavefront behaviour and properties, e.g., the number of wavefronts coming through the catheter and their different directions (Fig. 8(e)-(f)), the curved wavefronts due to potential re-entrant circuits (Fig. 8(b)) and even tissue anisotropy explained by small groups of clusters coming from the same place but moving into different directions, presumably following the cardiac fibres orientation (Fig. 8(a)).

Figure 8 here

Fig. 8: Examples of *loci maps* merged with its estimated activation map: (a) NSR, (b) ASR, (c) SAFW, (d) BT, (e) AFWF and (f) LB. LATs are color-coded from red (earliest) to pink (latest) in 10 ms isochrones. Electrodes are shown as empty circles and each focus solution $\mathbf{f}$

is shown in black dots connected with the center electrode of its corresponding 5×5 group. Spatial reference is shown with a cross.

4. Discussion:

Assessing LATs for activation mapping during AF is a common task to study and understand its underlying mechanisms [12]. Automatic LAT detection during AF relies in the detector accuracy and often requires manual checking. Moreover, LAT detection reduces the activation information to just a binary signal which takes values whether an activation is found, rejecting the remaining spatiotemporal information embedded in the morphology and time relation with adjacent electrodes.

In this paper, an integrated activation detection scheme is proposed, which takes benefit of the relation between u-EGMs, hence providing a spatiotemporal detection of activation maps in high-density recordings using MEA sensors. The rationale behind this technique is that it is possible to decompose a complete (and complex) activation pattern into a combination of simpler activation patterns fitted to small areas of the MEA sensor. The simplest activation pattern is concentric and isotropic, hence only depends on the location of the activation origin and the tissue conduction velocity.

The process introduces the parameters of the activation pattern into a UDL model of the tissue, deriving the corresponding u-EGM signals. Model pattern parameters were modified iteratively by comparing the resulting u-EGM signals against the recorded ones in order to reach a maximum of a cost function that takes into account the signal shape similarities and synchronization. Finally, the complete activation map is reconstructed by the weighted average of all solutions obtained by running this iterative process over the complete MEA sensor.

Mapping performance has been evaluated by comparing the estimated LATs with those obtained manually by an expert electrophysiologist in recordings during SR and AF. Additionally, activation maps were studied and classified based in a complexity scale, hence providing a more complete view of the method's behaviour and usefulness. Moreover, the complexity classification used in this work is similar to those activation modes recently identified by Kuklik and co-workers in an hypertensive sheep cardiac model [30].

During SR recordings, the agreement between manual and estimated LATs was proved to be very high. The error was -0.66 ± 2.00 ms with very high Spearman's correlation and Lin's concordance correlation factor ($\rho_s = 0.98$ and $\rho_c = 0.98$, $p < 0.01$ both). An exceptional situation was found in those recordings during SR. The cranial location of the MEA sensor over the right atrium (*RA4* recording) shows full abnormal atrial activity during SR. This activity suggests the presence of a re-entrant circuit, described by the proposed method, as illustrated in Fig. 5(b). Moreover, the novel proposed *loci maps* show potential trajectory of the activation wavefront evolution, suggesting the presence of a curved wavefront due to a functional re-entry present during SR (see Fig. 8(b)).

During AF recordings, the LAT estimation error was of -0.83 ± 6.02 ms with high agreement with manual annotations ($\rho_s = 0.93$ and $\rho_c = 0.90$, $p < 0.01$ both). This agreement is even higher considering the SAFW, BT and AFWF maps solely, which correspond to the 93 % of the studied maps. However, much lesser agreement was found in higher complexity maps (LB and CAF). Nevertheless, in this study those types of patterns were poorly represented in the available data (only at recording location *RA1*), limiting the conclusions that can be obtained from those classes.

462 Comparing the mean error in LAT estimation with the standard error of the mean, for
463 each atrial rhythm and atrial location, it is shown that the proposed method presents a
464 statistically significant bias. However, in 80 % of SR maps and 66 % of AF maps, this bias is
465 below one sampling interval and in 100 % of SR maps and 89 % of AF maps this bias is
466 below two sampling intervals. Moreover, it must be noted that having a systematic bias is not
467 crucial in activation mapping, where stability between the measurements at different sites is
468 pursued. This is quantified by the error standard deviation and the correlation with the
469 reference annotations.

470 The proposed algorithm provides smoother and more comprehensive activation maps
471 than those obtained manually as illustrated by Fig. 5. This fact is in concordance with the
472 smoothing nature of the weighted average process for reconstructing the final activation maps.
473 Additionally, the modelled activation pattern used for LAT estimation also contributes to this
474 smoothness. As an additional outcome of the iterative process, the *loci maps* appear to be an
475 interesting tool for assessing the activation behaviour and track the wavefront evolution in the
476 activation map under analysis. The presented algorithm for activation map and *loci map*
477 estimation was possible due to the iterative process and the small computation times of the
478 solid angle and UDL approaches, in contrast to the high computation times of more classic
479 and detailed tissue simulation approaches [17]. However, the proposed method needs manual
480 assistance to select the time interval to analyse the activation map; therefore, the presented
481 method is a semi-automatic approach.

482 The isotropic concentric activation model used in this work assumes the presence of a
483 single wavefront at the time of mapping within each 5x5 sensors analysis mask. This
484 assumption is not always accomplished and may be the reason behind the lower performance
485 observed in the more complex AF activity levels. Small lines of block or high frequency

(short wavelength) atrial activity may yield in poor estimation of the tissue conduction velocity or small values of the cost function due to the impossibility of the activation pattern to model the underlying activation behaviour. One possible solution is to select a smaller group of electrodes. Reducing the analysis mask size may allow to better estimate activations under those situations but also turns into a limitation because estimation of tissue conduction velocity could be less accurate and/or less robust to data acquisition errors (i.e., non-contact of electrodes) and noise.

Another limitation is related to the studied database. Only one set of locations coming from the same patient have been studied. It must be noted the singularity of the data used in this work, as epicardial high-density mapping is not performed during routine clinical interventions. Additionally, it must be noted also the fact that manual annotations and/or checking during AF of 124 channels is a high time-consuming task. Therefore, these constrain the database size for this study. However, more than 30000 LATs combining SR and AF recordings with very different propagation patterns were studied in this work, thus making a high amount of measurements for evaluating the proposed methodology. Nevertheless, extension of this work to more patients and more atrial locations is needed before clinical usage, especially including those left atrial locations where more complex activity can be expected.

5. Conclusion:

This paper presents an integrated spatiotemporal detection approach that allows to obtain smooth and comprehensive high-density activation maps and to track the underlying wavefront evolution. Simplified, but explicative enough, activation pattern and tissue models are used in order to generate u-EGM signals that resemble the measured activation map using an iterative process. Results indicate high accuracy of the proposed method compared against audited annotations during SR and AF. Therefore, although this work uses invasive data, it

opens the possibility of studying high-density activations maps with robust outcomes and the development of minimally invasive epicardial high-density mapping.

Acknowledgements:

This work is supported by personal grants to A.A. refs.: BES-2011-046644 and EEBB-I-13-06613, by project TEC2013-42140-R from Ministerio de Economía y Competitividad. Also by Aragón Government (Spain) and European Social Fund (EU) through Grupo Consolidado BSICoS ref.: T96 and by CIBER in Bioengineering, Biomaterials & Nanomedicine (CIBER-BBN) through Instituto de Salud Carlos III. The computation was performed by the ICTS 0707NAN-BIOSIS, by the High Performance Computing Unit of the CIBER in Bioengineering, Biomaterials & Nanomedicine (CIBER-BBN) at the University of Zaragoza

References:

[1] V. Fuster, L.E. Rydén, D.S. Cannom, H.J.G.M. Crijns, A.B. Curtis, K.A. Ellenbogen, et al., ACC/AHA/ESC 2006 Guidelines for the Management of Patients with Atrial Fibrillation, J. Am. Coll. Cardiol. 48 (2006) e149–e246.

[2] J. Friberg, B. Pernille, H. Scharling, N. Gadsbøll, G.B. Jensen, Rising Rates of Hospital Admissions for Atrial Fibrillation, Epidemiology. 14 (2003) 666–672.

[3] D. Mozaffarian, E.J. Benjamin, A.S. Go, D.K. Arnett, M.J. Blaha, M. Cushman, et al., Heart Disease and Stroke Statistics - 2015 Update: A Report From the American Heart Association, Circulation. 131 (2015) e29–e322.

[4] G.K. Moe, J.A. Abildskov, Atrial Fibrillation as a Self-Sustaining Arrhythmia Independent of Focal Discharge, Am. Heart J. 58 (1959) 59–70.

[5] M.A. Allessie, W.J.E.P. Lammers, F.I.M. Bonke, J. Hollen, Experimental Evaluation of Moe's Multiple Wavelet Hypothesis of Atrial Fibrillation, in: D.P. Zipes, J. Jalife

(Eds.), Card. Electrophysiol. Arrhythm., Grune & Stratton, 1985: pp. 265–276.

[6] K.T. Konings, C.J. Kirchhof, J.L.R.M. Smeets, H.J. Wellens, O.C. Penn, M.A. Allessie, High-Density Mapping of Electrically Induced Atrial Fibrillation in Humans, Circulation. 89 (1994) 1665–1680.

[7] M. Haïssaguerre, P. Jaïs, D.C. Shah, A. Takahashi, M. Hocini, G. Quiniou, et al., Spontaneous Initiation of Atrial Fibrillation by Ectopic Beats Originating in the Pulmonary Veins, N. Engl. J. Med. 339 (1998) 659–666.

[8] J. Eckstein, M. Kühne, S. Osswald, U. Schotten, Mapping of Atrial Fibrillation - Basic Research and Clinical Applications, Swiss Med. Wkly. 139 (2009) 496–504.

[9] G. Lee, S. Kumar, A. Teh, A. Madry, S. Spence, M. Larobina, et al., Epicardial Wave Mapping in Human Long-Lasting Persistent Atrial Fibrillation: Transient Rotational Circuits, Complex Wavefronts, and Disorganized Activity, Eur. Heart J. 35 (2014) 86–97.

[10] M.A. Allessie, N.M.S. de Groot, R.P.M. Houben, U. Schotten, E. Boersma, J.L.R.M. Smeets, et al., Electropathological Substrate of Long-Standing Persistent Atrial Fibrillation in Patients with Structural Heart Disease: Longitudinal Dissociation, Circ. Arrhythmia Electrophysiol. 3 (2010) 606–615.

[11] N.M.S. de Groot, R.P.M. Houben, J.L.R.M. Smeets, E. Boersma, U. Schotten, M.J. Schalij, et al., Electropathological Substrate of Long-Standing Persistent Atrial Fibrillation in Patients with Structural Heart Disease: Epicardial Breakthrough, Circulation. 122 (2010) 1674–1682.

[12] A. Yaksh, C. Kik, P. Knops, J.W. Roos-Hesselink, A.J.J.C. Bogers, F. Zijlstra, et al., Atrial Fibrillation: To Map or Not to Map?, Netherlands Hear. J. 22 (2014) 259–266.

[13] Z.F. Issa, J.M. Miller, D.P. Zipes, Clinical Arrhythmology and Electrophysiology: A Companion to Braunwald's Heart Disease, 2nd ed., Saunders, 2012.

[14] M.A. Allessie, N.M.S. de Groot, CrossTalk Opposing View: Rotors Have Not Been Demonstrated to be the Drivers of Atrial Fibrillation, J. Physiol. 592 (2014) 3167–3170.

[15] M.S. Spach, W.T. Miller, E. Miller-Jones, R.B. Warren, R.C. Barr, Extracellular Potentials Related to Intracellular Action Potentials During Impulse Conduction in Anisotropic Canine Cardiac Muscle, Circ. Res. 45 (1979) 188–204.

[16] T. Paul, J.P. Moak, C. Morris, A. Garson, Epicardial Mapping: How to Measure Local Activation?, Pacing Clin. Electrophysiol. 13 (1990) 285–292.

[17] O. Dössel, M.W. Krueger, F.M. Weber, M. Wilhelms, G. Seemann, Computational Modeling of the Human Atrial Anatomy and Electrophysiology, Med. Biol. Eng. Comput. 50 (2012) 773–799.

[18] M. Courtemanche, R.J. Ramirez, S. Nattel, Ionic Mechanisms Underlying Human Atrial Action Potential Properties: Insights From a Mathematical Model, Am. J. Physiol. - Hear. Circ. Physiol. 275 (1998) H301–H321.

[19] A. Nygren, C. Fiset, L. Firek, J.W. Clark, D.S. Lindblad, R.B. Clark, et al., Mathematical Model of an Adult Human Atrial Cell: The Role of K+ Currents in Repolarization, Circ. Res. 82 (1998) 63–81.

[20] A. van Oosterom, Solidifying the Solid Angle, J. Electrocardiol. 35 Suppl (2002) 181–192.

[21] A. Alcaine, N.M.S. de Groot, P. Laguna, J.P. Martínez, R.P.M. Houben, Estimation of High-Density Activation Maps During Atrial Fibrillation, in: Proc. Comput. Cardiol.,

Nice, France, 2015: pp. 825–828.

[22] R.P.M. Houben, N.M.S. de Groot, M.A. Allessie, Analysis of Fractionated Atrial Fibrillation Electrograms by Wavelet Decomposition, IEEE Trans. Biomed. Eng. 57 (2010) 1388–1398.

[23] D. Harrild, C. Henriquez, A Computer Model of Normal Conduction in the Human Atria., Circ. Res. 87 (2000) E25–E36.

[24] R.P.M. Houben, N.M.S. de Groot, J.L.R.M. Smeets, A.E. Becker, F.W. Lindemans, M.A. Allessie, S-wave Predominance of Epicardial Electrograms During Atrial Fibrillation in Humans: Indirect Evidence for a Role of the Thin Subepicardial Layer, Hear. Rhythm. 1 (2004) 639–647.

[25] A. van Oosterom, J. Strackee, The Solid Angle of a Plane Triangle, IEEE Trans. Biomed. Eng. BME-30 (1983) 125–126.

[26] P. V Bayly, B.H. KenKnight, J.M. Rogers, R.E. Hillsley, R.E. Ideker, W.M. Smith, Estimation of Conduction Velocity Vector Fields From Epicardial Mapping Data, IEEE Trans. Biomed. Eng. 45 (1998) 563–571.

[27] T.N. Fitzgerald, E.K. Rhee, D.H. Brooks, J.K. Triedman, Estimation of Cardiac Conduction Velocities Using Small Data Sets, Ann. Biomed. Eng. 31 (2003) 250–261.

[28] N. Mazeh, D.E. Haines, M.W. Kay, B.J. Roth, A Simplified Approach for Simultaneous Measurements of Wavefront Velocity and Curvature in the Heart Using Activation Times, Cardiovasc. Eng. Technol. 4 (2013) 520–534.

[29] L. Lin, A.S. Hedayat, B. Sinha, M. Yang, Statistical Methods in Assessing Agreement: Models, Issues, and Tools, J. Am. Stat. Assoc. 97 (2002) 257–270.

601 [30] P. Kuklik, D.H. Lau, A.N. Ganesan, A.G. Brooks, P. Sanders, High-Density Mapping
602 of Atrial Fibrillation in a Chronic Substrate: Evidence for Distinct Modes of Repetitive
603 Wavefront Propagation, Int. J. Cardiol. 199 (2015) 407–414.

604

Figure Legends:

Fig. 1: Schematic of the mapping procedure in posterior view: (a) Anatomical location of the MEA sensor in the atrium and (b) MEA sensor used for mapping procedure. CS: Coronary Sinus, CT: Crista Terminalis, IVC: Inferior Vena Cava, LA: Left Appendage, LBB: Left Bachmann Bundle, LPV: Left Pulmonary Vein, RA: Right Appendage, RBB: Right Bachmann Bundle, RPV: Right Pulmonary Vein, SVC: Superior Vena Cava.

Fig. 2: Schematic in: (a) perspective view and (b) lateral view, of the solid angle $\Omega_{\mathbf{e}_i}[n]$ obtained at electrode position $\mathbf{e}_i$ from a circular activation pattern $\mathbf{w}_{\mathbf{f},v}[n,\theta]$ subtended within a UDL shown as a closed grey strip.

Fig. 3: R-S difference evolution with distance to the activation focus: The u-EGM activation measured at point (a) has nearly QS morphology (R^{i}_{RS}=-0.9) that turns into a RS morphology as points (b) and (c) are distal from the source of activation (star). The grey dashed line indicates the zero level. Curved lines show the evolution of the activation wavefront with time in 5 ms steps.

Fig. 4: Schematic of the model optimization algorithm: signals are derived from the modelled propagation pattern in test and compared against the measured u-EGM signals. The algorithm decides a new focus location and the new pattern is tested. Direction vectors $\mathbf{r}_d$, $d = 1...4$, connect the center of each 2×2 corner group of electrodes G_d (indicated by dashed squares) to the activation focus $\mathbf{f}_l$. Vector $\mathbf{u}_{l+1}$ stands for the update vector for the next iteration. The signal amplitudes were scaled for visualization purposes as indicated in method section 2.4. Note: Characters with arrows appear boldface in text.

626 **Fig. 5:** Representative examples of the atrial activity complexity classification proposed in
627 this paper. Reference against estimated activation maps were shown in: (a) Normal sinus
628 rhythm (NSR) activity (error: -0.31 ± 0.93 ms, area: 100 %), (b) abnormal sinus rhythm
629 (ASR) activity (error: -0.23 ± 3.5 ms, area: 100 %), (c) single atrial fibrillation wavefront
630 (SAFW) activity (error: -0.03 ± 2.96 ms, area: 100 %), (d) breakthrough (BT) activity (error:
631 -0.27 ± 2.59 ms, area: 100 %), (e) atrial fibrillation wave fusion (AFWF) activity (error: -0.12
632 ± 1.73 ms, area: 100 %), (f) dissociated atrial activity due to a line of block (LB) (error: 0 ±
633 13.52 ms, area: 95.97 %) and (g) complex atrial fibrillation (CAF) activity (error: -5.3 ±
634 10.55 ms, area: 80.17 %). LATs are color-coded from red (earliest) to pink (latest) in 10 ms
635 isochrones. In case of no LAT could be identified at one electrode location, a cross is used.

636 **Fig. 6:** Agreement evaluation between reference and estimated LATs during SR: (a)
637 Reference vs. estimated LATs plot for Lin's concordance correlation factor ρ_c where pink
638 line indicates the unit slope and (b) Bland-Altman plot where red solid line indicates mean
639 error and red dashed lines show mean ± 2SD of the error.

640 **Fig. 7:** Agreement evaluation between reference and estimated LATs during AF at different
641 complexity levels including (a) SAFW, (b) BT, (c) AFWF, (d) LB (e) CAF and (f) all LATs
642 studied in this work. In each pair of panels, left shows reference vs. estimated LAT plot for
643 Lin's concordance correlation factor ρ_c (pink line indicates the unit slope) and the right panel
644 shows Bland-Altman plot (red solid line indicates mean error and red dashed lines show
645 mean ± 2SD of the error).

646 **Fig. 8:** Examples of *loci maps* merged with its estimated activation map: (a) NSR, (b) ASR,
647 (c) SAFW, (d) BT, (e) AFWF and (f) LB. LATs are color-coded from red (earliest) to pink
648 (latest) in 10 ms isochrones. Electrodes are shown as empty circles and each focus solution **f**

649 is shown in black dots connected with the center electrode of its corresponding 5×5 group.

650 Spatial reference is shown with a cross.

651

Figures

Figure 1:

Author: Alcaine et al.(Single Column, Black and white)

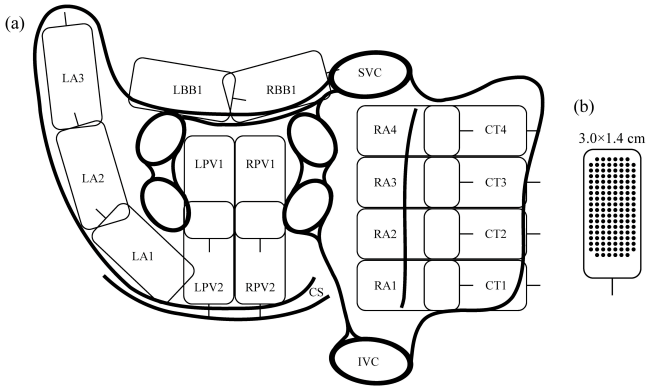

Figure 2:

Author: Alcaine et al. (Single Column, Black and white)

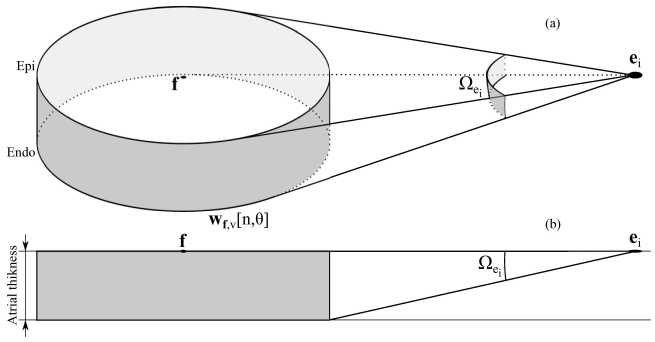

Figure 3:

Author: Alcaine et al. (Single Column, Black and white)

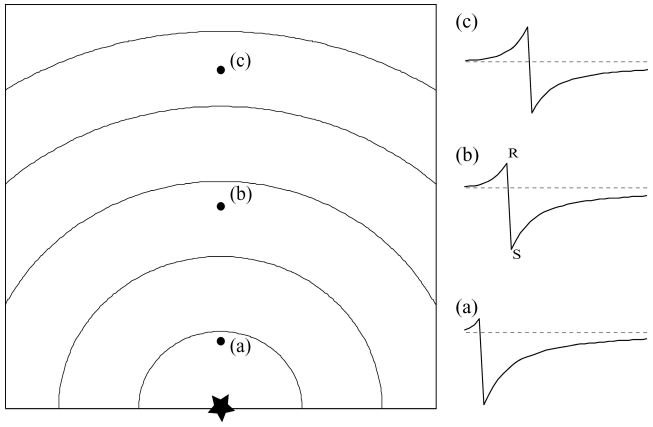

Figure 4:

Author: Alcaine et al. (Double Column, Black and white)

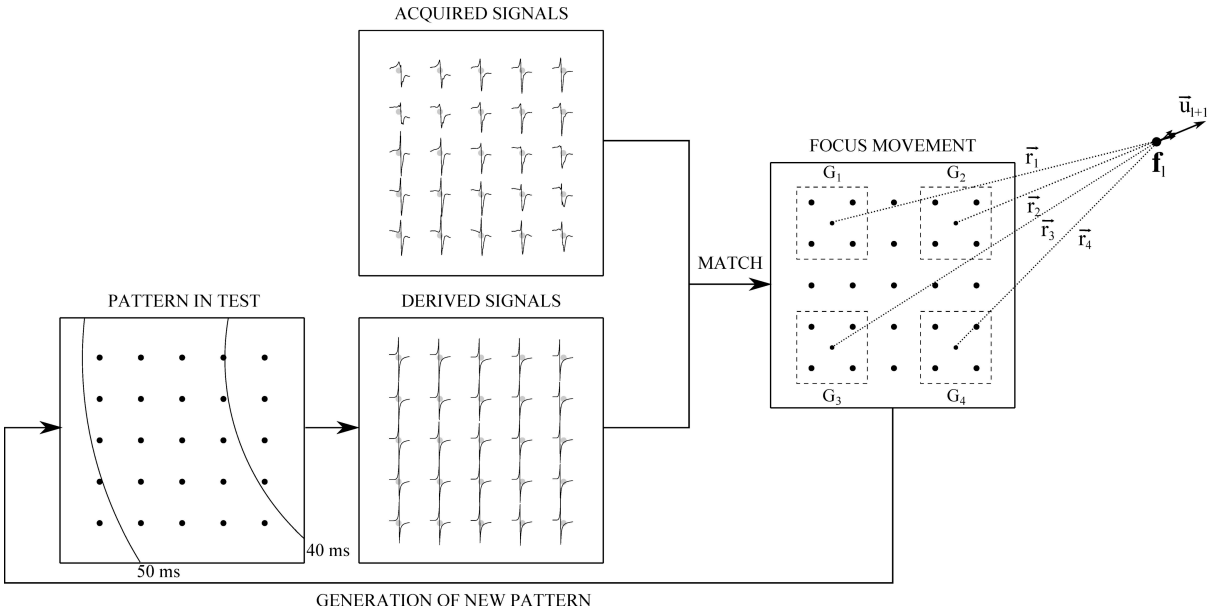

Figure 5:

Author: Alcaine et al. (Double Column, Colour figure on-line)

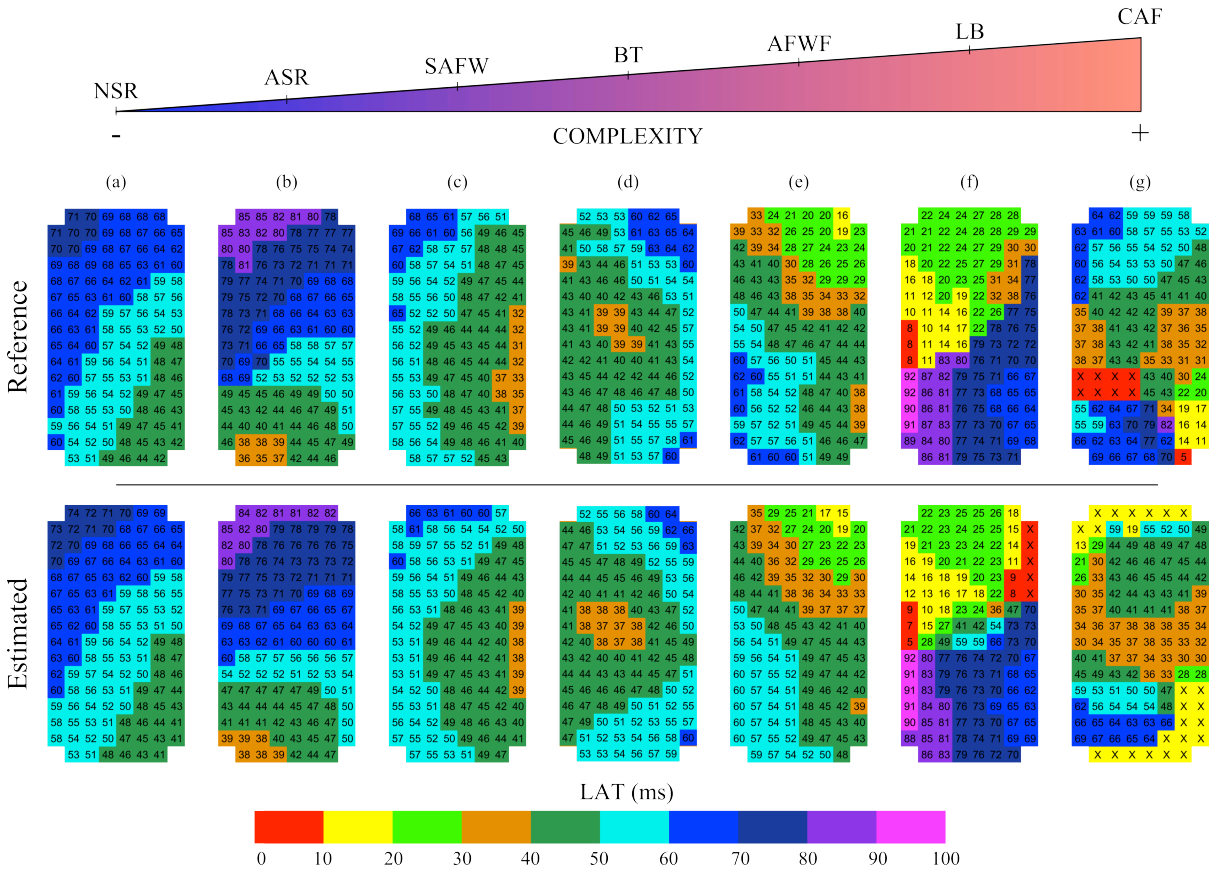

673 **Figure 6:**

674 *Author: Alcaine et al. (Single Column, Colour figure on-line)*

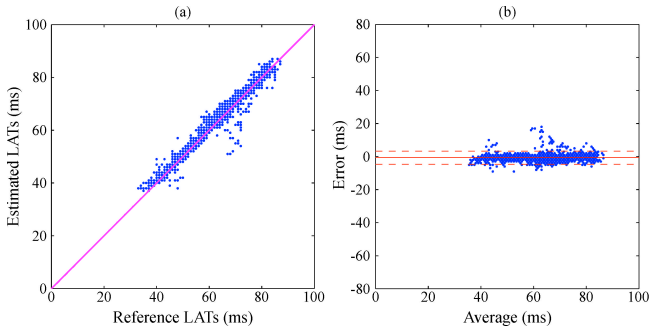

675

676

Figure 7:

Author: Alcaine et al. (Double Column, Colour figure on-line)

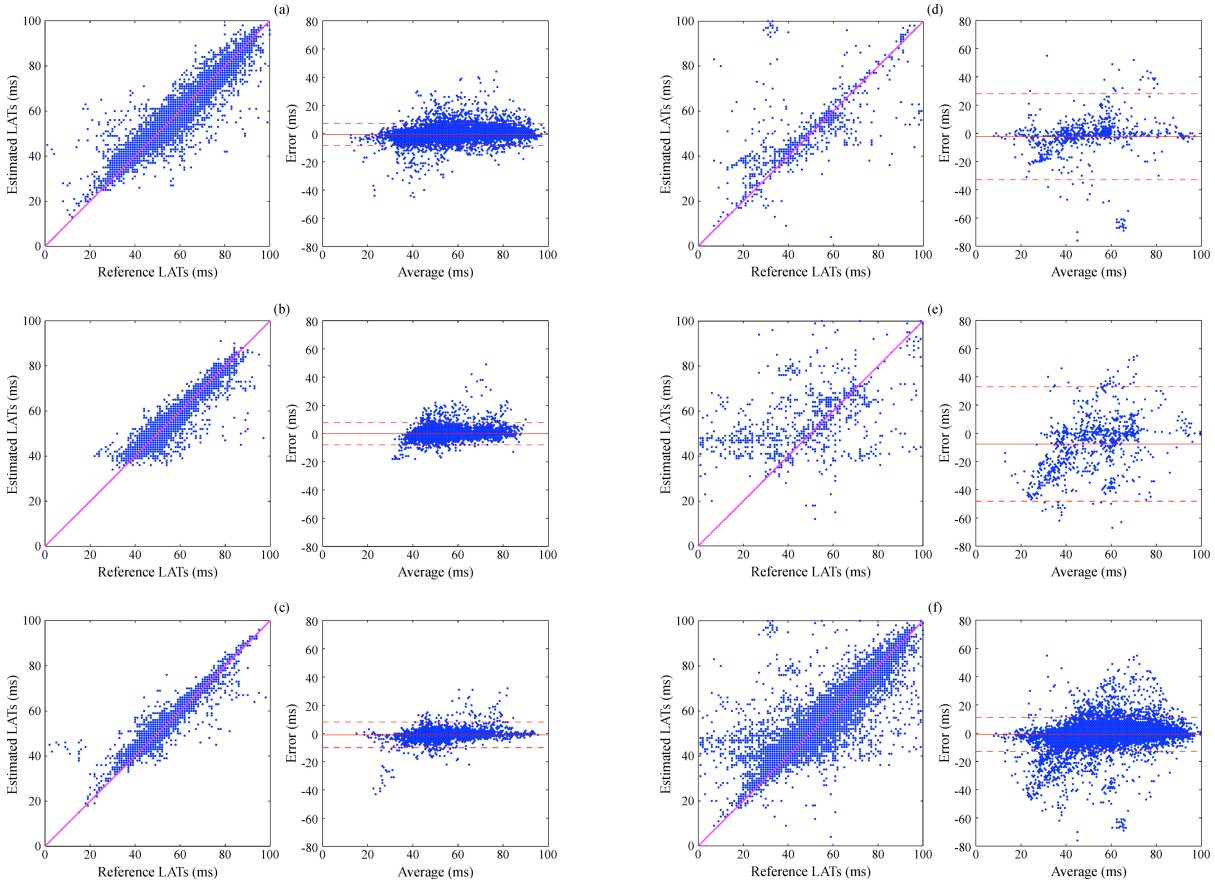

Figure 8:

Author: Alcaine et al. (Double Column, Colour figure on-line)

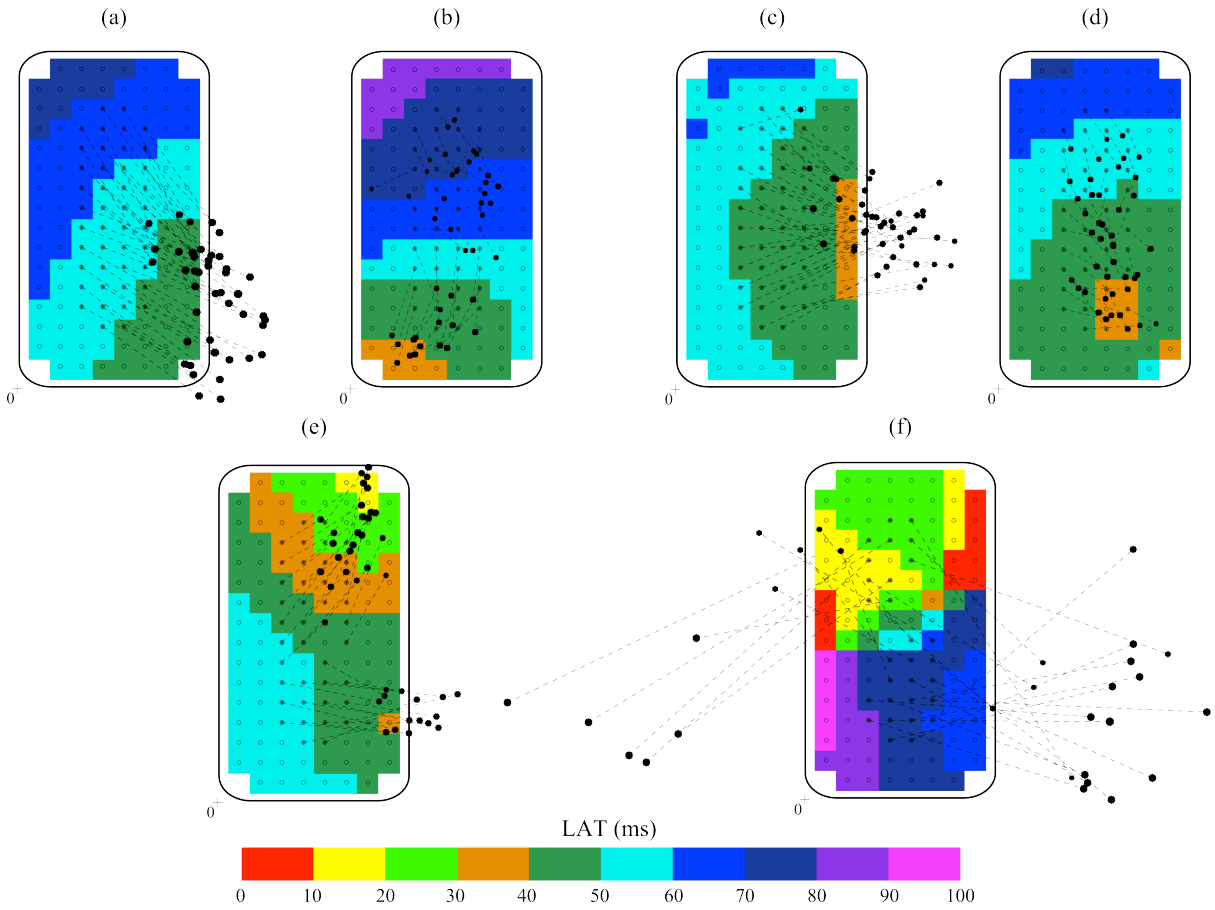

685 **Tables:**

686 **Table 1:** Detection error (mean ± SD), sensitivity and positive predictive value of comparing
687 estimated LATs with the manual reference in SR recordings. N/A stands for Not Applicable.

Loc.	Maps (#)	LATs (#)	Area (%)	Error (ms)	NSR (#)	ASR (#)	ρ_s	ρ_c	*Se* (%)	P^+ (%)
RA1	6	744	100	-0.82 ± 1.41	6	N/A	0.99*	0.99*	100	98.66
RA2	6	744	100	-0.78 ± 0.92	6	N/A	~1*	0.99*	100	100
RA3	6	744	100	-0.44 ± 0.76	6	N/A	~1*	~1*	100	100
RA4	7	868	100	-0.62 ± 3.36	N/A	7	0.97*	0.97*	100	93.43
Total	25	3100	100	-0.66 ± 2.00	18	7	0.98*	0.98*	100	97.84

688 * indicates a p - value < 0.01.

689

690 **Table 2:** Detection error (mean ± SD), sensitivity and positive predictive value of comparing
691 estimated LATs with the manual reference per AF recording at different levels of AF
692 complexity. N/A stands for Not Applicable.

Loc.	Type	Maps (#)	LATs (#)	Error (ms)	Area (%)	ρ_s	ρ_c	*Se* (%)	P^+ (%)
RA1	SAFW	27	3141	-1.05 ± 4.33	95.59 ± 13.98	0.95*	0.92*	95.42	92.87
	BT	3	350	-0.58 ± 4.74	97.62 ± 4.12	0.88*	0.80*	97.43	86.57
	AFWF	3	359	-1.91 ± 7.39	98.62 ± 1.71	0.90*	0.83*	98.26	78.55
	LB	7	789	-2.39 ± 15.25	91.70 ± 8.84	0.74*	0.67*	87.11	60.84
	CAF	10	903	-7.60 ± 20.26	83.36 ± 23.09	0.46*	0.38*	62.23	35.21
	Total	50	5542	-2.33 ± 11.01	92.91 ± 15.43	0.79*	0.68*	91.16	77.59
RA2	SAFW	44	5419	-1.09 ± 3.41	99.50 ± 1.81	0.96*	0.95*	99.47	93.17
	BT	2	238	-3.01 ± 3.61	100	0.95*	0.93*	100	81.51
	AFWF	15	1823	-1.09 ± 4.15	99.11 ± 1.66	0.95*	0.95*	99.04	90.78
	LB	N/A	N/A	N/A	N/A	N/A	N/A	N/A	N/A
	CAF	N/A	N/A	N/A	N/A	N/A	N/A	N/A	N/A
	Total	61	7480	-1.15 ± 3.63	99.42 ± 1.74	0.96*	0.95*	99.38	92.22
RA3	SAFW	15	1883	-0.12 ± 2.94	98.55 ± 2.00	0.97*	0.96*	98.48	95.64
	BT	43	5298	-0.11 ± 3.47	99.46 ± 0.96	0.95*	0.95*	99.41	92.26
	AFWF	2	242	0.22 ± 3.24	97.58 ± 3.42	0.92*	0.90*	97.38	92.15
	LB	N/A	N/A	N/A	N/A	N/A	N/A	N/A	N/A
	CAF	N/A	N/A	N/A	N/A	N/A	N/A	N/A	N/A
	Total	60	7373	-0.10 ± 3.33	99.17 ± 1.43	0.96*	0.96*	99.10	93.10
RA4	SAFW	53	6478	-0.16 ± 4.21	99.42 ± 1.41	0.96*	0.96*	99.35	87.90

	BT	4	488	0.92 ± 6.70	99.57 ± 0.48	0.84*	0.81*	99.51	83.20
	AFWF	7	865	-0.67 ± 3.95	99.88 ± 0.31	0.96*	0.94*	99.87	90.06
	LB	N/A	N/A	N/A	N/A	N/A	N/A	N/A	N/A
	CAF	N/A	N/A	N/A	N/A	N/A	N/A	N/A	N/A
	Total	64	7831	-0.14 ± 4.39	99.48 ± 1.30	0.96*	0.95*	99.42	87.84
all	SAFW	139	16871	-0.62 ± 3.90	98.61 ± 6.43	0.96*	0.96*	98.52	91.36
	BT	52	6374	-0.17 ± 3.94	99.38 ± 1.28	0.94*	0.94*	99.33	90.85
	AFWF	27	3289	-0.97 ± 4.54	99.14 ± 1.59	0.95*	0.93*	99.06	89.36
	LB	7	789	-2.39 ± 15.25	91.70 ± 8.84	0.74*	0.67*	87.11	60.84
	CAF	10	903	-7.60 ± 20.26	83.36 ± 23.09	0.46*	0.38*	62.23	35.22
	Total	235	28226	-0.83 ± 6.02	97.99 ± 7.66	0.93*	0.90*	97.80	88.36

693 * indicates a p - value < 0.01.

694

Vitae:

Alejandro Alcaine was born in Zaragoza, Spain, in 1986. Obtained the M.Sc. & B.Sc. in Telecommunication Engineering and the M.Sc. in Biomedical Engineering from the School of Engineering and Architecture at University of Zaragoza in 2011 and 2012, respectively.

Since 2012 he is working towards the Ph.D. degree in Biomedical Engineering supervised by Dr. Juan Pablo Martínez at Aragón Institute of Engineering Research (I3A) of University of Zaragoza thanks to a F.P.I. grant from the Ministry of Science and Innovation of Spanish Government. He is also a collaborator researcher at Centro de Investigación Biomedica en Red en Bioingeniería, Biomateriales y Nanomedicina (CIBER-BBN).

His research interest involve signal processing techniques applied to biological signals namely focused on its application to time-based detection and characterization of invasive intracardiac (EGM) signals for helping the guidance of the ablation procedures for arrhythmia treatment like atrial fibrillation or ventricular tachycardia.

Natasja M. S. de Groot received the Medical degree from Leiden University Medical School, Leiden, The Netherlands, in 1998, and the Ph.D. degree in 2006 from Maastricht University, Maastricht, The Netherlands.

She is currently Associate Professor and works as a cardiologist-electrophysiologist at the Department of Cardiology at the Erasmus Medical Center in Rotterdam. As a clinical electrophysiologist, she is specialized in 1) catheter ablation of tachycardias in patients with congenital heart disease, 2) catheter ablation in paediatric patients and 3) catheter ablation of complex tachyarrhythmias. She is chief of the research unit translational electrophysiology.

Her research projects are aimed at unravelling the pathophysiology of cardiac arrhythmias by a unique way of cardiac mapping in order to develop innovate diagnostic tools and therapies.

718 **Pablo Laguna** was born in Hoz de Jaca, Spain, in 1962. Received the M.S. degree in physics
719 and the Ph.D. from the Science Faculty at the University of Zaragoza, Zaragoza, Spain, in
720 1985 and 1990, respectively.

721 Currently, he is Full Professor of Signal Processing and Communications in the Department
722 of Electrical Engineering at the Engineering School, and a researcher at the Aragón Institute
723 for Engineering Research (I3A), both at the University of Zaragoza, also a member of the
724 Spanish Center for Biomedical Engineering, Biomaterial and Nano-medicine Research
725 CIBER-BBN. He has co-authored more than 130 research papers on this topic, over 260
726 international conference papers, and advise 12 Ph.D. Thesis. He has leaded a broad number
727 of projects on biomedical signal interpretation especially in the cardiovascular domain, most
728 of them with international collaborations at clinical and engineering places.

729 **Juan Pablo Martínez** was born in Zaragoza, Aragón, in 1976. He received the M.Sc. degree
730 in Telecommunication Engineering in 1999, and the PhD degree in Biomedical Engineering
731 in 2005, both at the University of Zaragoza.

732 Since 2000, he has been a lecturer and researcher in the Department of Electronic
733 Engineering and Communications, and the Aragon Institute of Engineering Research (I3A) of
734 the University of Zaragoza. He is currently an Associate Professor (Profesor Titular de
735 Universidad). From 2010 to 2014, he has been the Coordinator of the M.Sc. Program on
736 Biomedical Engineering.

737 His research activities are focused on Statistical Signal Processing methods to obtain clinical
738 information and risk indices from invasive and non-invasive cardiovascular signals.

739 **Richard P.M. Houben** has a long track record in biomedical research, development and
740 management of multidisciplinary research and development groups. His goal is always to

741 perform research and development efforts for the benefit of new and innovative products to
742 improve medical diagnostics and patient quality of life. He developed the ECG front-end for
743 the first digital implantable pacemaker and algorithms for accurate detection of atrial and
744 ventricular arrhythmias.

745 He is an active networker that has resulted in various successful research and development
746 programs and long lasting industrial and academic partnerships. He worked within
747 biomedical device industry for more than 25 years of which the last 20 years as a Scientist at
748 the Medtronic Bakken Research Center in Maastricht. He was awarded as a Medtronic
749 Technical Fellow and is a Senior Member of the IEEE. He is an expert in the interpretation of
750 biomedical signals with major applications in cardiology, neurology and diabetes. He holds
751 more than 20 patents and publications in highly ranked technical and medical journals.